2024 IEEE International Conference on Robotics and Automation (ICRA 2024)
May 13-17, 2024. Yokohama, Japan

A Soft Micro-Robotic Catheter for Aneurysm Treatment: A Novel Design and Enhanced Euler-Bernoulli Model with Cross-Section Optimization

Emanuele Nicotra[1], Chi Cong Nguyen[1], James Davies[1], Phuoc Thien Phan[1], Trung Thien Hoang[1], Bibhu Sharma[1], Adrienne Ji[1], Kefan Zhu[1], Trung Dung Ngo[2], Van Anh Ho[3], Hung Manh La[4], Nigel H. Lovell[1], *IEEE Fellow*, Thanh Nho Do[1,*], *IEEE Member*,

***Abstract*— Aneurysms, balloon-like bulges in blood vessels, present a significant health risk due to their potential to rupture, leading to life-threatening internal bleeding. Current treatments often involve delivering embolic materials or metal coils to fill these bulges, occluding them from the pressure of blood flow. However, clinical micro-catheters that deploy embolic materials used today face limitations, primarily their rigidity and the lack of active control over the bending tip of the catheter. This paper introduces a new soft micro-robotics catheter, with diameter of only 0.8 mm, equipped with a hollow channel. With this new design, the new device can induce bending motions at its tip for active steerability to reach desired aneurysm targets and then perform the delivery of embolic materials and tools. To enhance the control and precise navigation during procedures, a robust mathematical model and image processing techniques are also introduced and validated. Experiments are also performed to characterise and validate the model's accuracy and the steerability and navigation capabilities of the new micro-catheter.**

I. Introduction

Cerebral aneurysms are a pressing global health concern. With over 160 million affected worldwide, they lead to 500,000 deaths annually [1]–[3], and their prevalence is rising, with a growth rate surpassing 5% yearly [4]. Most of these aneurysms appear in vessels under 1.5 mm in diameter, and their rupture can lead to with devastating consequences: over half of the affected individuals may not survive, and many survivors grapple with lasting disabilities [5]–[7].

In addressing these vascular abnormalities, catheters play an indispensable role, especially in endovascular techniques. Though catheter designs have seen remarkable advancements, a persistent challenge is directing the catheter tip in-vivo. This limitation is particularly glaring when navigating winding vascular pathways or during precise coil deployments. Current embolization methods often utilize precurved-tip micro-catheter and guidewire for access, but once the guidewire is removed, the catheter tip cannot be steered inside the blood vessels, thus affecting deployment accuracy.

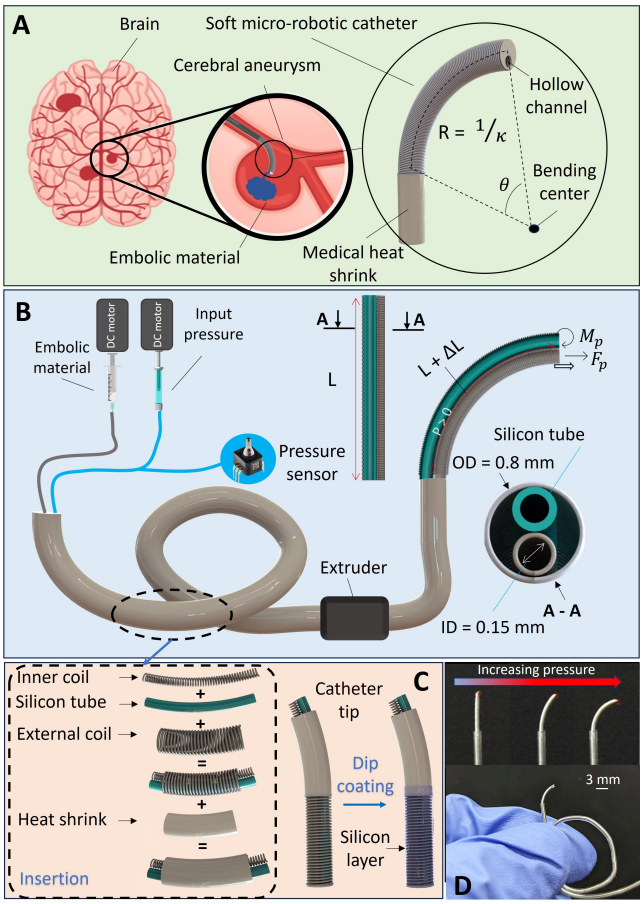

Fig. 1: Overview of the soft micro-robotic catheter. *a)* Its application to treat cerebral aneurysms. The robot navigates towards the aneurysm to deploy embolic material through the hollow channel; *b)* Working principle. The bending mechanism is illustrated in the lateral section view. The input pressure make the catheter bends. Cross-section view of the design; *c)* Overview of fabrication process, including insertion of the device components and dip-coating of the tip; *d)* Prototype of the soft micro-robotic catheter and its bending motions.

Recent innovations in remote-controlled catheter navigation have revolutionized endovascular surgery, enhancing safety and precision. Systems like the Sensei and Magellan

[1] The authors are with Graduate School of Biomedical Engineering, Faculty of Engineering, UNSW Sydney, Kensington Campus, NSW 2052, Australia. * Corresponding author, email: tn.do@unsw.edu.au
[2] The author is with More-Than-One Robotics Laboratory, Faculty of Sustainable Design Engineering, University of Prince Edward Island, Charlottetown, Canada.
[3] The author is with Soft Haptics Laboratory, School of Materials Science, Japan Advanced Institute of Science and Technology, Kawaguchi, Saitama, Japan.
[4] The author is with Department of Computer Science and Engineering, Advanced Robotics and Automation (ARA) Lab, University of Nevada, Reno, NV, USA,

have brought forth minimally invasive solutions, melding precision with operator expertise [8]. Yet, the ever-evolving landscape of endovascular surgery necessitates even more advanced catheter navigation systems. These systems must tackle challenges like miniaturization, intricate navigation, cost-efficiency, radiation reduction, and enhanced reliability [9], [10].

Soft robotics, given their flexibility and adaptability, are poised to advanced many fields such as wearable devices, haptics, and minimally invasive surgery [11]–[18]. The intricate human vasculature demands tools capable of navigating its challenging paths without causing harm. Soft robots, while still an emerging field, have the potential to minimize vessel perforation risks and tissue damage with their innate compliance. Their malleability allows for precision in even the most remote locations, offering superior control in endovascular and endoscopic procedures [19]–[25]. Several approaches have been proposed to fabricate soft or flexible actuators that can be used to control micro-catheter. The most notable approach is the use of magnetic field which wirelessly control the soft catheter tip [26]. However, this technique requires costly infrastructure (e.g., magnetic resonance imaging, bulky magnets, robotic arm, complex controller) to steer the catheter tip while limited at large size and small force. Other approaches include the use of pull-wire system such as Bowden cables or tendon sheath mechanisms [14], [27]–[31]. Despite advances, the use of pull-wire mechanisms limited the catheter at large size while they also are associated with high friction, nonlinear hysteresis, undesirable torsion, buckling, leading to undesirable tip motion that causes vascular damage and failure. Compared to these actuation technologies, hydraulically actuated soft robots potentially bring many benefits such as minimized footprint of actuators in the deflated state, biocompatibility in the case of leakage, and noninterference with intraoperative imaging. Furthermore, the integration of fluidic actuation into soft robots at the millimeter scale and smaller has demonstrated utility in the fabrication of increasingly complex actuators [32]. Yet, there are hurdles to overcome, such as the challenge of cross-section deformation during movement, which can significantly impact precision [33].

In this paper, we introduce a novel soft micro-catheter robot equipped with a hollow channel for embolization treatment. This device leverages the advantages of hydraulic artificial muscle [34], [35] technology to provide superior performance in aneurysm treatment. We will delve into the design, fabrication, and testing of our device, aiming to contribute to advancements in the field of robotic catheterization. We will discuss the theoretical modeling of the robot's behavior and the experimental validation of its performance. Through this comprehensive exploration, we aim to demonstrate the potential of our soft micro-catheter robot to contribute significantly to improved patient outcomes in aneurysm treatment. The aims of our proposed approach are: *a)* a novel fabrication method for soft continuum robots based on fluid actuation, which is easy to replicate, low cost and guarantees a reliable behaviour of the catheter; *b)* The incorporation of a hollow channel in the micro-catheter design, enabling the efficient delivery of embolization fluid to the target site; *c)* An enhanced mathematical model that leverages the Euler-Bernoulli (EB) beam theory with a cross-section shape optimization.

II. Materials and Methods

A. Overview of the soft micro-catheter

Figure 1 illustrates the comprehensive structure of the proposed micro-catheter. The robot's external body is constructed from medical heat shrink, which confines the entire structure with the exception of the flexible tip. This design allows for the predetermined specification of the actuated part's length. The latter is indeed capable of movement under the influence of internal pressure, supplied by a silicone rubber tube situated within the primary coil. Alongside the actuation chamber, a hollow channel exists, playing a crucial role in delivering the embolic material to the target site via the robot's body.

The deformation of the soft micro-catheter is achieved by applying pressure to the silicon tube, utilizing biocompatible fluids like saline water to ensure medical suitability. The heat shrink material, by design, restricts the robot's body from undergoing any deformation in response to input pressure, implying that only the robot's tip will be impacted by pressure variations. Furthermore, radial expansion is limited by the external coil, leading the tip to undergo two types of motion: axial elongation and planar bending. The elongation is a direct consequence of the resultant axial force. The bending motion, on the other hand, is facilitated by the offset between the pressure center within the silicone tube and the neutral axis of the composite cross-section. The bending principle will be thoroughly examined in section III, as it significantly influences the robot's behavior. Figure 1b) provides a visual representation of the soft micro-catheter's deformation principle. In addition to the deformation induced by input pressure, the robot must also possess the capability to navigate through body cavities. Therefore, the system's primary inputs are water pressure and linear displacement. With the ultimate objective of developing an autonomous robotic system, it is crucial to ensure that each input can be digitally controlled. Specifically, the input pressure is modulated by adjusting the linear displacement at the base of the syringe with a motorized linear slider (Zaber, model XLRQ150BL-E01, Zaber, Canada), while the robot's advancement is managed by a linear extruder (Flashforge Technology Co., Ltd, Cina).

The driving sources are mounted on a fixed board and connected to both a pressure sensor, connected to the fluid transmission tube by a T-connecter, and an encoder. These components will serve as integral elements of the low-level control system, providing real-time feedback for precise control and navigation.

B. Fabrication of the Soft Microcatheter

The soft micro-catheter's fabrication emphasizes simplicity, cost-effectiveness, and reliable robot behavior. Figure 1c)

summarizes the two main fabrication steps, including components insertion and the dip-coating of the tip. Specifically, position the external coil (Asahi Intecc Co., Ltd, Japan, OD = 0.8 mm, ID = 0.6 mm, length = 40 cm) under the microscope lens (Suba Engineering Pty Ltd, SubaScope200) and secure a thread inside a silicone rubber tube (Saint-Gobain S.A., France, OD = 0.6 mm, ID = 0.3 mm, length = 50 cm) using super glue (Loctiter ©, USA). Thread through the coil, securing both ends with tape. Dip coat the hollow channel (Asahi Intecc Co., Ltd, Japan, OD = 0.3 mm, ID = 0.15 mm, length = 50 cm) with Ecoflex-0030 (Smooth-On, Inc, USA) and thread it through the coil. Prepare a transmission tube (Microlumen Inc., USA, OD 0.3 mm, ID = 0.2 mm, length = 35 cm) and secure it inside the silicone tube with a knot and glue. Insert a needle (Element14 Pty Ltd, UK, OD = 34 G, ID = 0.095 mm) into the transmission tube, flushing with water. Adjust the coil's position, sealing the silicone tube's ends. Cover the coil with medical heat shrink (Element14 Pty Ltd, UK, Multicomp Pro, heat shrink ratio of 2:1, 1.1 mm), applying heat and sealing with glue. Post-glue drying, verify functionality using a syringe and a metal core (Asahi Intecc Co., Ltd, Japan, OD = 0.1 mm, length $>$ 50 cm). This method yields a 75 cm long soft micro-catheter with an OD = 0.8 mm and a 5 mm bending tip, primed for testing and use. Figure 1d) shows the prototype of the soft micro-robotic catheter and its bending motions.

III. Mathematical Model

The first step to model our micro-catheter consists in finding the induced deformation under the action of the input pressure. In the case of fluid-driven robots, [36] identifies EB beam theory and Finite Element as principal methods for fluid actuator modeling. This was explored further examining various design parameters' impact on a pneumatic network actuator [37] and studying the bending behavior of a Single Pneumatic Actuator under applied pneumatic pressure [38]. Finally, [39] presents validated analytical and finite-element models for soft fluidic actuators. To ensure clarity and rigor in our approach, in the following we detail the requisite assumptions and simplifications, necessary for the employment of the EB beam theory. The Boundary Value problem (BVP) is the most encompassing approach to describe the phenomenon of deformation. However, the complexity of the BVP often makes finding closed-form solutions to the systems of equations a challenging endeavor. Following the same line of reasoning as in [34], we assume that: 1) the inertia force of the fluid is negligible and can be disregarded; 2) the pressure is uniformly distributed; and 3) the helical coil, hollow channel, and tube experience identical displacements and share the same radius of curvature, a consequence attributable to the fabrication process. The actuation tube is the input of the system, and when pressurized it will transmit the stress to the other two components, and is assumed that each cross-section is a hollow circle tangent to the others. It follows that, for each component, the stress transmitted can be reduced to a force acting on the tip. Hence, each component can be reduced to beam loaded with a axial force and a torque acting on the tip. In particular the two springs (external coil and hollow channel) can be considered as beam by finding the equivalent Young's modulus E_{eq} from the spring constant k. Another remarkable fact is that each component's radial expansion is restricted. The metallic spring is inherently constrained, meaning that for both the external coil and the hollow channel, the only permissible deformations are axial elongation and bending. For the silicone tube, we assume that it retains its cross-sectional shape, which is yet to be determined. By construction, the loading does not excite out-of-plane motions and the cross-section of each component, and of the whole robot, is symmetric with respect to the plane of loading. Therefore the problem can be simplified to the Timoshenko beam. Lastly, since there cannot be matter penetration or separation and vertical strain among the components, every vertical vincular reactions must be balanced at every point along the robot, it follows that shear deformations are negligible. Consequently, for each component, the BVP eventually simplifies to the EB beam as each cross-sectional plane is rigid (i.e., there is no strain in the plane of the cross-section). Solving the EB beam problem for each component leads to the expression of the elongation and curvature, respectively

$$\epsilon_i = \frac{F_i}{E_i A_i} \tag{1}$$

$$\kappa_i = \frac{M_i}{E_i I_i} \tag{2}$$

Where F_i and M_i are the axial load and tip torque of the i-th component (1 = external coil, 2 = silicon tube, 3 = hollow channel), while E_i, A_i and I_i are the Young's modulus, cross-section area and second moment of inertia, respectively. It follows that we expect a constant curvature behaviour for each component. Furthermore, the rigidity of every cross-sectional plane implies that the entire catheter's cross-section is also a rigid plane. In conclusion the problem can be analyzed as a single EB beam with a composite cross-section.

A. Robot Dependent Mapping

A significant benefit of the constant-curvature model is its ability to decompose kinematics into two distinct mappings [40]. The first mapping transitions from the actuator space to the configuration space parameters, which describe constant-curvature arcs. This mapping is specific to the robot under consideration. The second mapping transitions from this configuration space to the task space, represented in Cartesian coordinates. This space curve describes the position and orientation along the robot's backbone and is independent of the specific robot. For our case, the main focus is on the robot dependent mapping, however we will conclude the section with the final map between the input pressure and the tip position and orientation.

1) Solution for Nominal Cross-Section: The external force acting on the system is given by the input pressure p inside the silicone tube, namely $F_p = pA_p$, where A_p is the internal area of the tube. The latter needs to be balanced

by the internal force, which is the sum of the forces of each component, given by the solution of the BE problem

$$F_p = \sum_i F_i = \sum_i A_i E_i \epsilon_i \tag{3}$$

Using the solution of the EB beam for each component 1 and imposing the condition that the elongation is the same for each component we get the expression of the total elongation of the robot

$$\epsilon = \frac{pA_p}{\sum_i A_i E_i} \tag{4}$$

The bending moment acting on the tip of the robot is given by $M_p = F_p e$, where $e := y_p - \bar{y}$ is the difference between the pressure center inside the silicone tube y_p and the neutral axis of the composite cross-section $\bar{y}$, as illustrated in Figure 2a). The neutral axis is the position on the cross-section where the sum of the axial forces is zero. By imposing the condition, the neutral axis is given by

$$\bar{y} = \frac{\sum_i E_i \bar{y}_i A_i}{\sum_i E_i A_i} \tag{5}$$

where $\bar{y}_i$ is the centroid of the i-th cross-section. Finally, using the solution of the EB beam 2 and imposing the moment balance and constant curvature for each component, the expression of the curvature of the robot can be found

$$M_p = \sum_i M_i = \sum_i E_i I_i \kappa_i \tag{6}$$

$$\kappa = \frac{pA_p(y_p - \bar{y})}{\sum_i E_i I_i} \tag{7}$$

In conclusion the bending of the robot is highly dependent on the offset between the center of pressure and the neutral axis, which depend themselves on the shape assumed by the silicone tube other than the material properties of each component.

2) Shape Optimization: As shown in the previous section, the solution of the problem is very sensitive to the shape assumed by the cross-section of the silicone tube. For this reason we want to find the shape that better approximate the real behaviour of the for the robot. We then relax some constraints in order to have to free parameters directly related to the shape of the tube, and to find their value by solving an optimization problem. By construction the space occupied by the tube is constrained vertically by the presence of the hollow channel and the external coil, which by assumption cannot experience radial deformations. However, nothing constrains the expansion of the silicone tube in the other directions, and, given the assumption of evenly distributed pressure, the resulting shape of the tube cross-section is approximated as an hollow ellipse. Moreover, again for the constrain on the radial expansion of the hollow channel and external coil, it is reasonable to assume that the input pressure will tend to squeeze the silicone tube in the vertical direction; Also, due to the nature of the bending motion, we expect a smaller wall thickness the further from the bending center; for these reasons, we let the thickness of the shape to be non-constant. In order to capture this behaviour we

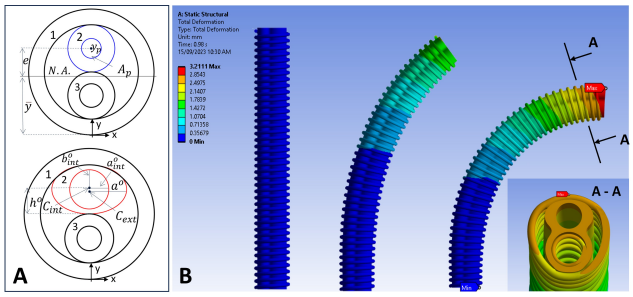

Fig. 2: *a)* Nominal (*top*) and optimized ellipse(*bottom*) cross-sections; *b)* Ansys simulation of the bending tip.

model the shape of the silicone tube as the result of the subtraction of a full ellipse of semi-axis a and b "minus" a hollow ellipse of semi-axis a_{int} and b_{int}. We then allow the two ellipse to be not concentric, meaning that the center of the hollow ellipse can be shifted along the vertical direction, making possible to have a varying thickness of the wall of the silicone tube. In conclusion, the the only fixed parameter is b since we want the tube to be tangent to both the external coil and the hollow channel at the same time. The four parameters are gathered in single variable $x := [a, a_{int}, b_{int}, h] \in \mathbb{R}^4$ and they are found by solving the following optimization problem

$$\min_{x \in \mathbf{X}} \quad w_\epsilon \left(\epsilon(x) - \epsilon_d\right)^2 + w_\kappa \left(\kappa(x) - \kappa_d\right)^2 \tag{8}$$

where $\epsilon(x) : \mathbb{R}^4 \longrightarrow \mathbb{R}$ and $\kappa(x) : \mathbb{R}^4 \longrightarrow \mathbb{R}$ are two functions given by 4 and 7 written as a function of x; ϵ_d and κ_d are the real values of the elongation and curvature; w_ϵ and w_κ are two scalar weight; $\mathbf{X} \subset \mathbb{R}^4$ is the domain of x given by geometric constraints. In conclusion, the solution of the optimization problem $x^o = [a^o, a^o_{int}, b^o_{int}, h^o]$ gives the optimal value of the parameters that better approximate the real shape of the silicon tube, which are used to find the elongation $\epsilon^o(p)$ and curvature $\kappa^o(p)$, as functions of the input pressure only.

B. Robot Independent Mapping

To complete the model we consider also the robot independent mapping, that relates the curvature of the robot and the tip length L to the tip position $[x_t, y_t]$ and orientation $\theta := \kappa L$, which is represented by the homogeneous transformation $T \in SE(3)$. The function $f : \mathbb{R} \longrightarrow SO(3)$ that relates the input pressure to the tip position and orientation is then the composition $f(p) := T(\theta^o(p)) =$

$$\begin{bmatrix} -\sin\theta^o(p) & \cos\theta^o(p) & 0 & L^o \dfrac{(1-\cos\theta^o(p))}{\theta^o(p)} \\ \cos\theta^o(p) & \sin\theta^o(p) & 0 & L^o \dfrac{\sin\theta^o(p)}{\theta^o(p)} \\ 0 & 0 & 1 & 0 \\ 0 & 0 & 0 & 1 \end{bmatrix} \tag{9}$$

where $\theta^o = \kappa^o(p) L^o(p)$, with $\kappa^o(p)$ and $L^o(p)$ given by the solution of the optimization problem in 8

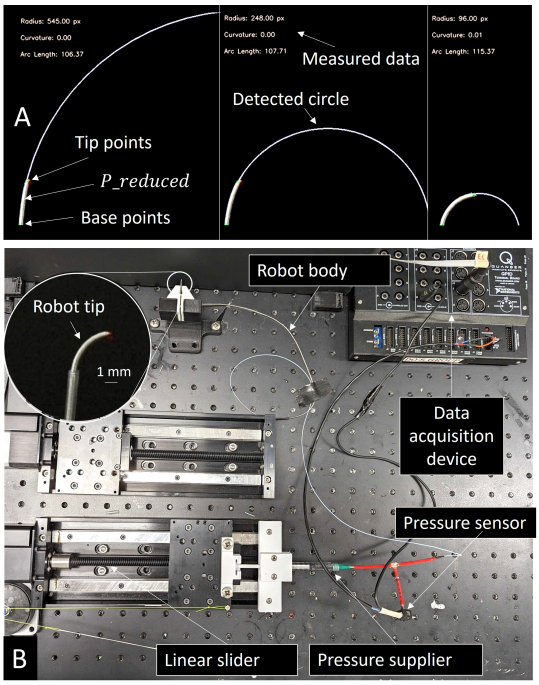

Fig. 3: *a)* Three consecutive examples of the image processing measurement. The robot behaves as a perfect arc of a circle at every time instant; *b)* Experimental setup for the robot characterization;

IV. Experimental validation

1) Model Validation: In order to validate the kinematic model of the soft micro-catheter we collected pressure and curvature data and compared them against the developed robot dependent mapping. The input pressure is measured with the mentioned pressure sensor, while the output elongation and curvature are measured using image processing techniques. In the proposed method, images are acquired using a Nikon D7500 DSLR (Nikon D7500, Japan) camera and undergo a series of preprocessing steps facilitated by OpenCV. These steps include conversion to grayscale, Gaussian blurring, and binary thresholding. The resulting binary image serves as the basis for edge detection, which employs the Canny algorithm. This allows us to isolate the structural boundaries of the robot, by populating a set with the detected points (x_i, y_i) with $i = 0, 1, 2, ..., n$. To facilitate robust detection, the tip of the robot is colored distinctly in red. A Hue, Saturation, and Value (HSV) color space transformation is performed on the original image, followed by a specific masking operation. The mask is designed to filter only the red regions in the image. The coordinates of the pixels within this red region are averaged to find the tip's location, (x_t, y_t). The primary goal is to compute the curvature of the robot based on its shape. To achieve this, the coordinates of the robot's edges are fitted to a circle using a least squares optimization method. The problem is formulated as:

$$\min_{x_c, y_c, r} \sum_{i=1}^{n} \left(\sqrt{(x_i - x_c)^2 + (y_i - y_c)^2} - r \right)^2$$

where x_c and y_c are the coordinates of the circle's center, r is the radius, and (x_i, y_i) are the coordinates of the edge points. The curvature, κ, is then computed as the reciprocal of the radius r, i.e., $\kappa = \frac{1}{r}$.

To mitigate computational complexity while retaining the essential geometric features of the robot, a point reduction technique is employed. Specifically, the edge-detected image, which initially contains a plethora of points outlining the robot, is sub-sampled. Given an original set of edge points $\mathcal{P} = \{(x_1, y_1), (x_2, y_2), \ldots, (x_n, y_n)\}$, the image is divided into horizontal slices, each of height Δy, which is a tunable parameter. For each slice, the mean of the x-coordinates of the points falling within that slice is computed, resulting in a reduced set of points $\mathcal{P}_{\text{reduced}}$. The reduced set is formulated as:

$$\mathcal{P}_{\text{reduced}} = \left\{ \left(\frac{1}{N_i} \sum_{j=1}^{N_i} x_{j,i}, y_i \right) \right\}_{i=1}^{M}$$

where N_i is the number of points in the i-th slice and M is the total number of slices. The reduced set of points, $\mathcal{P}_{\text{reduced}}$, simplifies the subsequent least-squares optimization problem for circle fitting, thereby reducing computational overhead in case real-time measurements are desired.

Finally, the arc length of the robot is calculated by measuring the angular displacement between the robot's base and tip around the circle's center. The arc length, L, can be formulated as:

$$L = r \left| \theta_{\text{t}} - \theta_{\text{b}} \right|$$

where θ_{t} and θ_{b} are the angular positions of the tip and the base of the robot, respectively, relative to the circle's center. The code also provides visual feedback by overlaying the detected edges, fitted circle, and curvature information on the original video frames. An example of the image processing algorithm's output is illustrated in Figure 3a).

For the robot's characterization, the results, including radius, curvature, and arc length, are stored in a CSV file for subsequent data analysis in MATLAB. This involves filtering and cleaning the raw data and applying the shape optimization. In our study, we employed a low-pass Infinite Impulse Response (IIR) filter to process both the input and output data. The filter was designed with a passband frequency of 0.5 Hz, a stopband frequency of 1 Hz, a passband ripple of 1 dB, and a stopband attenuation of 20 dB and the sample rate was set to 200 Hz. Figure 4 depict the system's response to a sinusoidal input pressure.

After solving the shape optimization problem 8, the final output compares the data and the model prediction. Figure 2a) represents the predicted shape of the cross-section, making evident how the tube, not being constrained, finds its optimal shape by enlarging the horizzontal semiaxis of the ellipse. The results are confirmed also by a physics simulation performed in Ansys (Ansys, Inc., USA). Figure 2b) shows how the designed tip bends with constant curvature under the input pressure, and with a cross-section

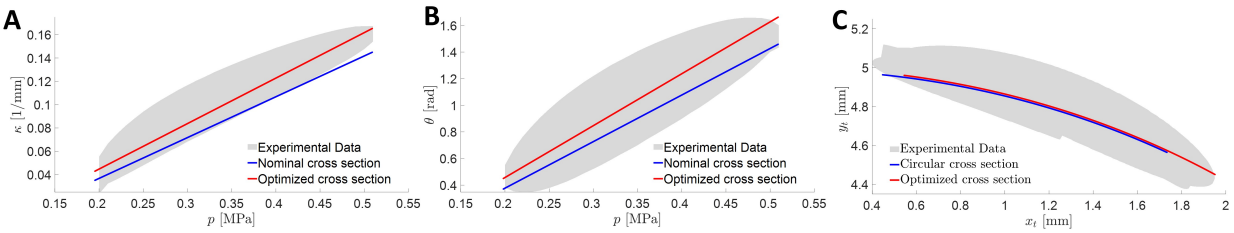

Fig. 4: System response to sinusoidal input pressure repeated for 10 cycles. Data are generated with the Zaber console applying a sine-wave to the motorized linear slider attached to the base of the syringe. An hystersis cycle emerges form the characterization of the device, however the model is able to predict the hysteresis trend for the curvature (*a*)), bending angle (*b*)) and plane position obtained from the kinematic model (*c*)).

that resemble the result of optimization. Figure 4 demonstrates the benefits of shape optimization for a better fit with the collected data compared to the nominal circular cross-section. The comparison of the NRMSE between the nominal and optimized cross-section, specifically in relation to the hysteresis trend, underscores the advantages of our optimization approach ($\text{NMRSE}_n/\text{NMRSE}_o = 20.1371$). The initial conditions of the optimization are sampled from a grid search bounded by the geometric constraints of the robot's cross-section. In conclusion, despite the presence of significant hysteresis, the proposed model accurately predicts the trend of the hysteresis loop with final optimal parameters $x^o = [0.23, 0.12, 0.12, 0.55]\text{mm}$.

2) Phantom Navigation: In our concluding demonstration, we showcase the proficiency of our device in seamlessly navigating through a blood vessel phantom. Given the robot's planar bending capabilities, the phantom is structured to be planar, ensuring all its branches are discernible from an overhead perspective. The ideal phantom is both transparent and flexible, for this reason the material chosen for the 3D printing process is the elastic 50A resin (elongation at break = 160 %, tensile strength = 3.2 MPa, tear strength = 19.1 kN/m). Figure 5 encapsulates the essence of the navigation experiment. The robot is teleoperated towards the desired target, and deploys the embolic material. The operator, leveraging visual feedback, can control both the linear progression and the bending of the catheter, ensuring the robot accurately reaches the designated target. This initial validation underscores the potential for more intricate navigation and enhanced autonomy of the robot in future applications.

V. Conclusion and Future Works

In this work, we introduced a novel soft micro-catheter robot. Our aspiration is to push toward a broader adoption of soft robotic catheters, ultimately replacing the conventional rigid or pre-bent alternatives. Our innovative fabrication technique, rooted in fluid actuation, not only ensures cost-effectiveness and reproducibility but also guarantees the catheter's dependable performance. The integration of a hollow channel in the design is a testament to our commitment to enhancing the efficiency of embolization fluid delivery.

Our mathematical model, anchored in the Euler-Bernoulli beam theory and augmented with a shape optimization

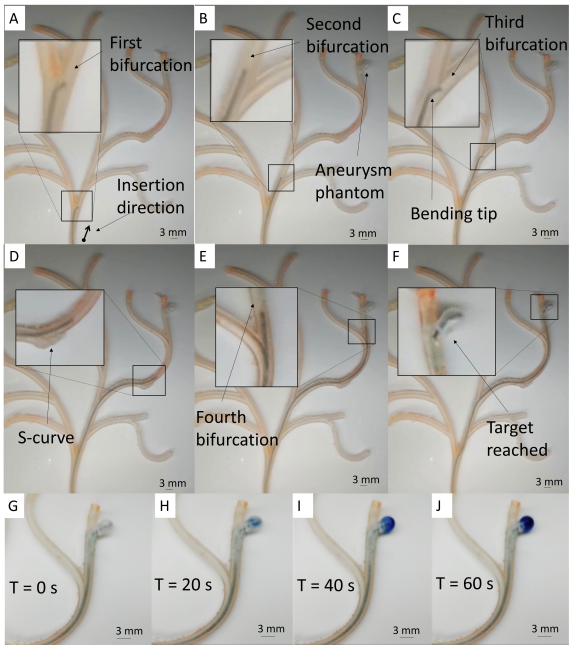

Fig. 5: Demonstration of the device *(a-f)* Process of the catheter navigation; *(g-j)* Embolic material injection

approach, offers an accurate model of the robot's kinematics. This model, validated through experimental characterization, has shown remarkable accuracy in predicting the robot's behavior. Nevertheless, while the model can anticipate the cyclical trend, it does not adequately capture the hysteresis observed during bending. Addressing this hysteresis remains a challenge and necessitates further refinement.

Looking ahead, this paper is intended as a foundational step for subsequent research endeavors. Our future work will focus on augmenting the robot's actuators to at least three, enabling omnidirectional bending. This enhancement, while maintaining the same design, fabrication, and modeling techniques, will further push the boundaries of what our robot can achieve. Additionally, we aim to integrate in-situ force sensing, advanced users' interface, and delve deeper into the robot's navigation capabilities, with an emphasis on scaling the levels of autonomy [41]–[43], ensuring its seamless integration into clinical workflows and broadening its applicability in diverse medical scenarios.

REFERENCES

[1] A. I. Qureshi, V. Janardhan, R. A. Hanel, and G. Lanzino, "Comparison of endovascular and surgical treatments for intracranial aneurysms: an evidence-based review," *The Lancet Neurology*, vol. 6, no. 9, pp. 816–825, 2007.

[2] G. J. E. Rinkel, M. Djibuti, A. Algra, and J. Van Gijn, "Prevalence and risk of rupture of intracranial aneurysms: a systematic review," *Stroke*, vol. 29, no. 1, pp. 251–256, 1998.

[3] B. A. Foundation. (2020) Brain aneurysm statistics. [Online]. Available: https://bafound.org/about-brainaneurysms/brain-aneurysm-basics/brain-aneurysm-statistics-and-facts/

[4] M. H. Vlak, A. Algra, R. Brandenburg, and G. J. Rinkel, "Prevalence of unruptured intracranial aneurysms, with emphasis on sex, age, comorbidity, country, and time period: a systematic review and meta-analysis," *The Lancet Neurology*, vol. 10, no. 7, pp. 626–636, 2011.

[5] A. Keedy, "An overview of intracranial aneurysms," *McGill Journal of Medicine: MJM*, vol. 9, no. 2, p. 141, 2006.

[6] S. Juvela, M. Porras, and O. Heiskanen, "Natural history of unruptured intracranial aneurysms: a long-term follow-up study," *Journal of Neurosurgery*, vol. 79, no. 2, pp. 174–182, 1993. [Online]. Available: https://pubmed.ncbi.nlm.nih.gov/8331397/

[7] S. Juvela, K. Poussa, H. Lehto, and M. Porras, "Natural history of unruptured intracranial aneurysms: a long-term follow-up study," *Stroke*, vol. 44, no. 9, pp. 2414–2421, 2013. [Online]. Available: https://pubmed.ncbi.nlm.nih.gov/23868274/

[8] L. Cruddas, G. Martin, and C. Riga, "Robotic endovascular surgery: Current and future practice," *Seminars in Vascular Surgery*, vol. 34, pp. 233–240, 2021.

[9] P. Chen, Y. Wang, D. Tian, Y. Guo, and K. Xu, "The catheter and guidewire operating systems of vascular interventional surgical robots: A systematic review," *IEEE Trans. Med. Robot. Bionics*, pp. 1–1, 2023.

[10] S. Gunduz, H. Albadawi, and R. Oklu, "Robotic devices for minimally invasive endovascular interventions: A new dawn for interventional radiology," *Advanced Intelligent Systems*, vol. 3, p. 2000181, 2021.

[11] M. Cianchetti, C. Laschi, A. Menciassi, and P. Dario, "Biomedical applications of soft robotics," *Nature Reviews Materials*, vol. 3, no. 6, pp. 143–153, 2018.

[12] M. T. Thai, P. T. Phan, T. T. Hoang, S. Wong, N. H. Lovell, and T. N. Do, "Advanced intelligent systems for surgical robotics," *Advanced Intelligent Systems*, vol. 2, no. 8, p. 1900138, 2020.

[13] M. T. Thai, P. T. Phan, T. T. Hoang, H. Low, N. H. Lovell, and T. N. Do, "Design, fabrication, and hysteresis modeling of soft microtubule artificial muscle (smam) for medical applications," *IEEE Robotics and Automation Letters*, vol. 6, no. 3, pp. 5089–5096, 2021.

[14] H. M. Le, T. N. Do, and S. J. Phee, "A survey on actuators-driven surgical robots," *Sensors and Actuators A: Physical*, vol. 247, pp. 323–354, 2016.

[15] M. T. Thai, T. T. Hoang, P. T. Phan, N. H. Lovell, and T. N. Do, "Soft microtubule muscle-driven 3-axis skin-stretch haptic devices," *IEEE Access*, vol. 8, pp. 157 878–157 891, 2020.

[16] P. T. Phan, T. T. Hoang, M. T. Thai, H. Low, J. Davies, N. H. Lovell, and T. N. Do, "Smart surgical sutures using soft artificial muscles," *Scientific reports*, vol. 11, no. 1, p. 22420, 2021.

[17] P. T. Phan, M. T. Thai, T. T. Hoang, J. Davies, C. C. Nguyen, H.-P. Phan, N. H. Lovell, and T. N. Do, "Smart textiles using fluid-driven artificial muscle fibers," *Scientific reports*, vol. 12, no. 1, p. 11067, 2022.

[18] J. Davies, M. T. Thai, T. T. Hoang, C. C. Nguyen, P. T. Phan, H.-P. Phan, N. H. Lovell, and T. N. Do, "A stretchable filament sensor with tunable sensitivity for wearable robotics and healthcare applications," *Advanced Materials Technologies*, vol. 8, no. 6, p. 2201453, 2023.

[19] K.-W. Kwok, H. Wurdemann, A. Arezzo, A. Menciassi, and K. Althoefer, "Soft robot-assisted minimally invasive surgery and interventions: Advances and outlook," *Proc. IEEE*, vol. 110, pp. 871–892, 2022.

[20] J. Burgner-Kahrs, D. C. Rucker, and H. Choset, "Continuum robots for medical applications: A survey," *IEEE Transactions on Robotics*, vol. 31, no. 6, pp. 1261–1280, 2015.

[21] M. T. Thai, P. T. Phan, H. A. Tran, C. C. Nguyen, T. T. Hoang, J. Davies, J. Rnjak-Kovacina, H.-P. Phan, N. H. Lovell, and T. N. Do, "Advanced soft robotic system for in situ 3d bioprinting and endoscopic surgery," *Advanced Science*, vol. 10, no. 12, p. 2205656, 2023.

[22] C. C. Nguyen, S. Wong, M. T. Thai, T. T. Hoang, P. T. Phan, J. Davies, L. Wu, D. Tsai, H.-P. Phan, N. H. Lovell, *et al.*, "Advanced user interfaces for teleoperated surgical robotic systems," *Advanced Sensor Research*, vol. 2, no. 4, p. 2200036, 2023.

[23] C. C. Nguyen, M. T. Thai, T. T. Hoang, J. Davies, P. T. Phan, K. Zhu, L. Wu, M. A. Brodie, D. Tsai, Q. P. Ha, *et al.*, "Development of a soft robotic catheter for vascular intervention surgery," *Sensors and Actuators A: Physical*, vol. 357, p. 114380, 2023.

[24] T.-K. Nguyen, S. Yadav, T.-A. Truong, M. Han, M. Barton, M. Leitch, P. Guzman, T. Dinh, A. Ashok, H. Vu, *et al.*, "Integrated, transparent silicon carbide electronics and sensors for radio frequency biomedical therapy," *ACS nano*, vol. 16, no. 7, pp. 10 890–10 903, 2022.

[25] T. N. Do, T. E. T. Seah, and S. J. Phee, "Design and control of a mechatronic tracheostomy tube for automated tracheal suctioning," *IEEE Transactions on Biomedical Engineering*, vol. 63, no. 6, pp. 1229–1238, 2015.

[26] K. J. Hwang, J. and H. Choi, "A review of magnetic actuation systems and magnetically actuated guidewire-and catheter-based microrobots for vascular interventions," *Intelligent Service Robotics*, vol. 13, pp. 1–14, 2020.

[27] T. N. Do, T. Tjahjowidodo, M. W. S. Lau, and S. J. Phee, "Nonlinear friction modelling and compensation control of hysteresis phenomena for a pair of tendon-sheath actuated surgical robots," *Mechanical Systems and Signal Processing*, vol. 60, pp. 770–784, 2015.

[28] A. Pal, V. Restrepo, D. Goswami, and R. V. Martinez, "Exploiting mechanical instabilities in soft robotics: Control, sensing, and actuation," *Advanced Materials*, vol. 33, no. 19, p. 2006939, 2021.

[29] T. N. Do, T. Tjahjowidodo, M. W. S. Lau, and S. J. Phee, "Adaptive control of position compensation for cable-conduit mechanisms used in flexible surgical robots," in *2014 11th International Conference on Informatics in Control, Automation and Robotics (ICINCO)*, vol. 1. IEEE, 2014, pp. 110–117.

[30] V. Hassani, T. Tjahjowidodo, and T. N. Do, "A survey on hysteresis modeling, identification and control," *Mechanical systems and signal processing*, vol. 49, no. 1-2, pp. 209–233, 2014.

[31] T. N. Do, T. Tjahjowidodo, M. W. S. Lau, and S. J. Phee, "Position control of asymmetric nonlinearities for a cable-conduit mechanism," *IEEE Transactions on Automation Science and Engineering*, vol. 14, no. 3, pp. 1515–1523, 2015.

[32] D. Van Lewen, T. Janke, H. Lee, R. Austin, E. Billatos, and S. Russo, "A millimeter-scale soft robot for tissue biopsy procedures," *Advanced Intelligent Systems*, vol. 5, p. 2200326, 2023.

[33] M. Russo, S. Sadati, X. Dong, A. Mohammad, I. Walker, C. Bergeles, K. Xu, and D. Axinte, "Continuum robots: An overview," *Advanced Intelligent Systems*, vol. 2200367, 2023.

[34] P. Phan, M. Thai, T. Hoang, N. Lovell, and T. Nho Do, "Hfam: Soft hydraulic filament artificial muscles for flexible robotic applications," *IEEE Access*, vol. 8, pp. 226 637–226 652, 2020.

[35] P. T. Phan, T. T. Hoang, M. T. Thai, H. Low, N. H. Lovell, and T. N. Do, "Twisting and braiding fluid-driven soft artificial muscle fibers for robotic applications," *Soft Robotics*, vol. 9, no. 4, pp. 820–836, 2022.

[36] B. Gorissen, D. Reynaerts, S. Konishi, K. Yoshida, J.-W. Kim, and M. De Volder, "Elastic inflatable actuators for soft robotic applications," *Adv. Mater.*, vol. 29, p. 1604977, 2017.

[37] W. Hu, R. Mutlu, W. Li, and G. Alici, "A structural optimisation method for a soft pneumatic actuator," *Robotics*, vol. 7, p. 24, 2018.

[38] N. Gariya, P. Kumar, R. S. Bangari, and M. Makkar, "Bending analysis of a soft pneumatic actuator using analytical and numerical methods," *Materials Today: Proceedings*, p. S2214785323036647, 2023, in Press.

[39] P. Polygerinos, Z. Wang, J. T. B. Overvelde, K. C. Galloway, R. J. Wood, K. Bertoldi, and C. J. Walsh, "Modeling of soft fiber-reinforced bending actuators," *IEEE Transactions on Robotics*, vol. 31, pp. 778–789, 2015.

[40] I. Robert J. Webster and B. A. Jones, "Design and kinematic modeling of constant curvature continuum robots: A review," *The International Journal of Robotics Research*, vol. 29, no. 13, pp. 1661–1683, 2010.

[41] A. Pore, Z. Li, D. Dall'Alba, A. Hernansanz, E. De Momi, A. Menciassi, A. Casals Gelpí, J. Dankelman, P. Fiorini, and E. V. Poorten, "Autonomous navigation for robot-assisted intraluminal and endovascular procedures: A systematic review," *IEEE Trans. Robot.*, pp. 1–20, 2023.

[42] S. Peng, S. Wu, Y. Yu, Z. Sha, G. Li, T. T. Hoang, M. T. Thai, T. N. Do, D. Chu, and C. H. Wang, "Carbon nanofiber-reinforced strain sensors with high breathability and anisotropic sensitivity," *Journal of Materials Chemistry A*, vol. 9, no. 47, pp. 26 788–26 799, 2021.

[43] M. T. Thai, J. Davies, C. C. Nguyen, P. T. Phan, T. T. Hoang, A. Ji, K. Zhu, B. Sharma, E. Nicotra, T. T. Vo-Doan, *et al.*, "Soft wearable haptic display and flexible 3d force sensor for teleoperated surgical systems," *Advanced Sensor Research*, vol. 3, no. 1, p. 2300105, 2024.